remote sensing

MDPI

Technical Note

Estimation of Aerosol Extinction Coefficient Using Camera Images and Application in Mass Extinction Efficiency Retrieval

Juseon Shin [1], Dukhyeon Kim [2] and Youngmin Noh [3,*]

[1] Division of Earth Environmental System Science, Pukyong National University, Busan 48513, Korea; juseonshin@pukyong.ac.kr
[2] School of Basic Science, Hanbat National University, Daejeon 34158, Korea; dhkim7575@hanbat.ac.kr
[3] Department of Environmental Engineering, Pukyong National University, Busan 48513, Korea
* Correspondence: nym@pknu.ac.kr; Tel.: +82-051-629-6526

Abstract: In this study, we attempted to calculate the extinction parameters of $PM_{2.5}$ using images from a commercial camera. The photo pixels provided information on the characteristics of the objects (i.e., the reflectivity, transmittance, or extinction efficiency) and ambient brightness. Using the RGB values of pixels, we calculated the extinction coefficient and efficiency applied to the mass concentration of $PM_{2.5}$. The calculated extinction coefficient of $PM_{2.5}$ determined from the camera images had a higher correlation with the $PM_{2.5}$ mass concentration (R^2 = 0.7) than with the visibility data, despite the limited mass range. Finally, we identified that the method of calculating extinction parameters using the effective wavelength of RGB images could be applied to studies of changes in the atmosphere and aerosol characteristics. The mass extinction efficiency of $PM_{2.5}$, derived from images, and the mass concentration of $PM_{2.5}$ was (10.8 $\pm$ 6.9) $m^2\ g^{-1}$, which was higher than the values obtained in Northeast Asia by previous studies. We also confirmed that the dry extinction efficiency of $PM_{2.5}$, applied with a DRH of 40%, was reduced to (6.9 $\pm$ 5.0) $m^2\ g^{-1}$. The extinction efficiencies of $PM_{2.5}$, calculated in this study, were higher than those reported in previous other studies. We inferred that high extinction efficiency is related to changes in size or the composition of aerosols; therefore, an additional long-term study must be conducted.

Keywords: camera; mass extinction efficiency; visibility; extinction coefficient

check for updates

Citation: Shin, J.; Kim, D.; Noh, Y. Estimation of Aerosol Extinction Coefficient Using Camera Images and Application in Mass Extinction Efficiency Retrieval. *Remote Sens.* **2022**, *14*, 1224. https://doi.org/10.3390/rs14051224

Academic Editor: Simone Lolli

Received: 27 January 2022
Accepted: 26 February 2022
Published: 2 March 2022

Publisher's Note: MDPI stays neutral with regard to jurisdictional claims in published maps and institutional affiliations.

Copyright: © 2022 by the authors. Licensee MDPI, Basel, Switzerland. This article is an open access article distributed under the terms and conditions of the Creative Commons Attribution (CC BY) license (https://creativecommons.org/licenses/by/4.0/).

1. Introduction

Atmospheric aerosols, one of the most critical pollutants suspended in the atmosphere, have received increasing attention owing to their adverse impacts on air quality and human health [1,2]. Suspended particulate matter with an aerodynamic diameter less than 2.5 µm ($PM_{2.5}$) in atmospheric aerosols are more closely associated with adverse health effects than the larger particles. Therefore, the 2006 World Health Organization Air Quality Guidelines recommended $PM_{2.5}$, rather than PM_{10}, as an indicator of air pollution from particulate matter, which has increasingly become a public concern worldwide [3]. The World Health Organization (WHO) recently decreased the standard limit, in the Air Quality Guidelines, of $PM_{2.5}$ from 10 to 5 $\mu g\ m^{-3}$ due to the increasing impact of $PM_{2.5}$ on air pollution over time [4].

$PM_{2.5}$ can be distributed at various altitudes and over long distances in the air. Therefore, various remote sensing technologies, such as satellites, light detection and ranging (lidar), and sun photometers are used to measure the concentrations and distributions of particulate matter in the atmosphere as well as on the ground [5–8]. Remote sensing technologies have many spatiotemporal advantages, but they also have significant disadvantages. Satellites provide information over a wide area; however, confirming detailed data within a narrow region of several kilometers is challenging. Temporal resolutions also require long intervals, that is, daily (polar-orbiting satellites) and hourly (geostationary-orbiting satellites) [9–12]. The lidar technique is a valuable active remote sensing device that provides concentration data over a distance, but it mainly detects vertical distribution depending on altitude. Although lidar sometimes detects horizontal distributions, it has limitations due to eye safety and topographical factors. In general, optical measurement methods (lidar, optical particle counters, visibility systems, and nephelometers) calculate the optical concentration using transmittance or scattering methods, which require improved accuracy in the signal-to-noise ratio (SNR). Furthermore, remote sensing techniques have limited applications as they are cost and skill intensive.

Furthermore, aerosols in the atmosphere can change rapidly; hence, prediction or measurement methods must be developed for real-time data [13,14]. Therefore, there is a need for improving the spatial and temporal resolution of the national aerosol monitoring systems (for PM_{10} and $PM_{2.5}$). From a scientific perspective, continuous monitoring of the mass extinction efficiency (MEE) is crucial as it depends on the type of aerosol irrespective of the mass quantities.

To overcome the limitations of remote sensing technology and obtain information on air quality effectively, we used landscape images to analyze visibility [15–22]. Many studies have attempted to measure visibility change [18–20,22] and aerosol optical depth [23] using the RGB information of the images; however, they have not calculated the extinction coefficient of aerosols. The RGB values of landscape or sky images change due to the extinction coefficient and scattering properties of aerosols, object position, the position between the sun and the camera, atmospheric cloud conditions, and other parameters such as the sensitivity and transmittance of the imaging optics in the measurement. Therefore, we aimed to confirm the applicability of monitoring aerosols using images from a commercial camera to provide a practical and uncomplicated method to overcome the limitations of remote sensing and existing measurement systems.

In this study, we calculated the aerosol extinction coefficient using the images captured by a commercial camera and compared it with the mass concentration of $PM_{2.5}$, and the retrieved extinction coefficient from the visibility data, to validate data reliability. In addition, the extinction efficiency of $PM_{2.5}$ was calculated using the extinction coefficient and mass concentration of $PM_{2.5}$.

2. Materials and Methods

2.1. Calculation of the Extinction Coefficient from the Camera Images

We calculated the extinction coefficient from the camera-image files according to the method developed by Kim and Noh [24]. The imaged pixels include information on the reflectance of the target object, transmittance or extinction/scattering/absorption efficiency, and brightness in the atmosphere. Thus, the intensity, $I\,(D_i)$, of the image incident on a given pixel can be described by Equation (1) [25–27]:

$$I(D_i) = C_1 e^{-\alpha D_i} + C_2(1 - e^{-\alpha D_i}) = (C_1 - C_2)e^{-\alpha D_i} + C_2 \tag{1}$$

where D_i is the distance from the target object (i) to the camera, C_1 is the light intensity of the target object itself, α is the average extinction coefficient between the target object and the camera, and C_2 is the atmospheric scattering light scattered by the particulate matter. C_1 is only affected by the characteristics of the scattering objects (i.e., the reflectivity and sun–camera angle) and not by the distance. The first term in Equation (1) represents the intensities scattered from the objects that decrease exponentially depending on the distance between the objects. The second term describes the amount of scattered light from the particulate matter and air molecules, which increases with the distance of the target.

Equation (1) demonstrates the possibility of calculating the image-extinction coefficient (α_{IMAGE}) based on the following assumptions: (1) C_1 and C_2 are located at different distances in the same direction in a single image; (2) a known pixel value, $\mathrm{I}\,(\mathrm{D_i})$, of the target object exists with similar scattering characteristics; and (3) C_1 is constant regardless of distance because it is not sensitive to the scattering angle from the sun and camera. Therefore, mountains with similar characteristics and inclinations are the proper target objects.

The critical factor in determining C_2 is the scattering angle, which depends on the sun, object, and camera. In addition, C_2 is dependent on the scattering phase functions related to the properties of aerosol particles, such as size, shape, and refractive index. However, the scattering of particles is constant when the target objects are positioned in the same direction. Thus, the C_2 values of two pixels extracted from different objects in the same direction are similar.

Obtaining targets in the exact same direction as a single image, from actual observation, is challenging. In most of the cases in this study, we used target objects in similar directions because the differences in the object angles were within the range of systematic error. Finally, we calculated the extinction coefficient of the objects in a single image. The steps for selecting the pixel value, $I\ (D_i)$, of the target object through the best analysis conditions were as follows: (1) the objects with similar directions (for example, a mountain in this study) were selected, (2) the specific areas at the same distance (D_1, D_2, ... , D_5 in Figure 1a) were selected, and (3) the average or minimum values of all pixels in the selected area were determined. The sky was considered an object with a reflectance close to zero because no real object was present.

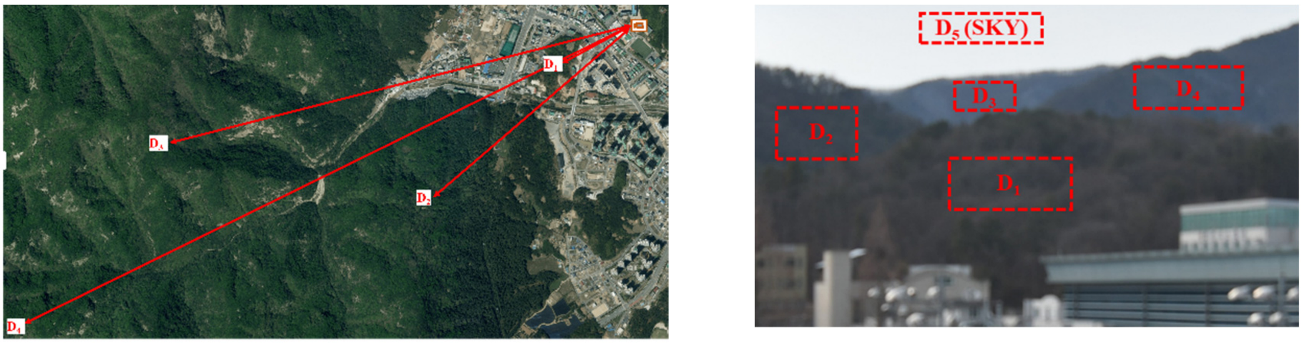

(**a**) (**b**)

Figure 1. Observation points: (**a**) distance between the camera and the mountain and (**b**) planes of the measured image.

Figure 1a shows four mountains composed of similar ecosystems, and the distances to D_1, D_2, D_3, D_4, and D_5 are 0.4, 1.4, 2.4, 3.5, and 10 km, respectively. The red boxes denote the point pixels of the objects on the image of the mountain from the camera. We selected the smallest values among all of the pixels inside the boxes and considered them as $I\ (D_i)$ from their average. The intensities of the RGB wavelengths were calculated from the pixels of the images. Kim and Noh [24] confirmed that the calculated and measured intensities of RGB are highly correlated and developed a method to calculate the effective RGB wavelength (λ_i) by considering the RGB sensor characteristics of a digital camera, as follows:

$$\lambda_i = \frac{\int_{-\infty}^{\infty} \lambda S_i(\lambda) I(\lambda) \varepsilon(\lambda) d\lambda}{\int_{-\infty}^{\infty} S_i(\lambda) I(\lambda) \varepsilon(\lambda) d\lambda}, \quad i = R,\ G, \text{ and } B \tag{2}$$

In Equation (2), $S_i\ (\lambda)$ is the intensity of the digital camera for RGB sensors and $I(\lambda)$ is the light intensity spectrum that varies with time and region. In this instance, $\varepsilon(\lambda)$ is the change in extinction efficiency from aerosol properties, such as size, refractive index, and wavelength [28]. Although the effective wavelength of RGB depends on unknown parameters, such as the Mie scattering effect, three effective wavelengths can be obtained from a given solar intensity and sensitivity characteristic profile, $S_i\ (\lambda)$. The effective wavelengths of camera RGB are 597 nm, 534 nm, and 459 nm, respectively; these have differences but are similar to the wavelength of 550 nm when we calculate the visual range. This study used a high-resolution monochromator to calculate the sensitivity profiles.

2.2. Calculation of the Extinction Coefficient and Efficiency Using Visibility Data

We compared the two extinction coefficient values calculated from the visibility data and camera images. The extinction coefficient (α_{VIS}) was derived from the Koschmieder equation [29].

$$\alpha_{VIS}\left(\mathrm{km}^{-1}\right) = -\frac{ln\varepsilon}{VIS(\mathrm{km})} \quad (3)$$

VIS indicates visibility and ε is the brightness contrast threshold. We set ε as 0.02, which is commonly used by the WHO. Equation (3) calculates the extinction coefficient of ambient conditions. To determine the extinction coefficient of $PM_{2.5}$, we used Equation (4), considering the mass loading of $PM_{2.5}$ and PM_{10} (in µg m^{-3}), and NO_2 concentrations (in ppb) [30].

$$\alpha_{VIS2.5}\left(\mathrm{M\,m}^{-1}\right) = \frac{3912}{VIS(\mathrm{km})} - 0.6(\mathrm{PM}_{10} - \mathrm{PM}_{2.5}) - 10 - 0.33\mathrm{NO}_2 \quad (4)$$

The first term represents the total extinction coefficient (at 550 nm) computed from the visual range (km) using Koschmieder's formula. The other terms (subtracting factors not related to the $PM_{2.5}$ extinction coefficient) correspond to the extinction contribution of coarse particles, the Rayleigh scattering of air molecules, and the absorption of ambient NO_2 molecules. The constants were calculated using empirical studies [31–33]. We also applied Equation (4) to calculate the extinction coefficient of $PM_{2.5}$ ($\alpha_{IMAGE2.5}$) from the camera images, excluding NO_2 concentration (ppb) and the effect of the mass loading of the particulate matter with a diameter of over 2.5 µm.

Finally, we calculated the mass extinction efficiency of $PM_{2.5}$ ($\alpha_{eff2.5}$) by dividing the mass concentration ($PM_{2.5}$) from the extinction coefficient of $PM_{2.5}$ obtained from the camera images ($\alpha_{IMAGE2.5}$) or visibility data ($\alpha_{VIS2.5}$), based on the following equation:

$$\alpha_{eff2.5}\left(\mathrm{m}^2\,\mathrm{g}^{-1}\right) = \frac{\alpha_{VIS2.5\ or\ IMAGE2.5}\left(\mathrm{Mm}^{-1}\right)}{\mathrm{PM}_{2.5}(\mu\mathrm{g\,m}^{-3})} \quad (5)$$

2.3. Measurement Period and Site

We captured the images from the fourth floor of the School of Art and Design building at Hanbat National University, Daejeon, Republic of Korea (36.34°N, 127.30°E), in the west–southwest direction every day from February 7 to 28, 2021. This step was conducted at one-hour intervals from 08:00 to 18:00 h in local time (LT). In this study, all time values are in LT. We excluded data when the weather conditions seriously affected visibility, such as rainfall, snowfall, and fog. We obtained 193 images during the entire measurement period (22 days). The mass concentration of $PM_{2.5}$ was obtained from the nearest observatory (the rooftop of the Noeun 1-dong community service center; 36.37°N, 127.32°E) available on the national real-time air pollution level public website (www.airkorea.or.kr (retrieved 15 March 2021)) managed by the Korea Environment Corporation. The visibility and relative humidity data were obtained from the Daejeon Regional Meteorological Administration (36.37°N, 127.37°E), which was located 6.8 km to the northeast of Hanbat National University. We presented all measurement sites in Figure 2.

Figure 2. Measurement station and observatory of the PM and visibility information. Site 1: the Daejeon Regional Meteorological Administration (36.37°N, 127.37°E); Site 2: Hanbat National University (36.34°N, 127.30°E); and Site 3: Noeun 1-dong community service center (36.37°N, 127.32°E).

3. Results and Discussion

3.1. Extinction Coefficient

The mass concentration and extinction coefficient, measured by the camera images and visibility data, of $PM_{2.5}$ at one-hour intervals during the measurement period are shown in Figure 3. We ignored the effect of coarse particles because their contribution to extinction is relatively lower than fine particles [34–36]. Measurements were obtained from basin regions where urban pollutants dominate; therefore, we assumed that the contribution of coarse particles to extinction would be less than 30% [37]. The $PM_{2.5}$ mass concentration was high on 7, 11–15 February, and was over 30 μg m^{-3} on the 19–21. The maximum value was 63.5 μg m^{-3} at 11:00 h on 7 February. The $\alpha_{IMAGE2.5}$ values show similar trends with the mass concentration of $PM_{2.5}$. On 7 February, when the $PM_{2.5}$ mass concentration was the highest, $\alpha_{IMAGE2.5}$ was also high (0.22–0.95 km^{-1}). In addition, $\alpha_{IMAGE2.5}$ was low (0.006–0.22 km^{-1}) on 8–9 and 16–18 February. The maximum and minimum values of $\alpha_{IMAGE2.5}$ were 0.95 and 0.002 km^{-1}, respectively. The $\alpha_{VIS2.5}$ values had few similarities with the change in $PM_{2.5}$ concentration, except on 7 February. The maximum and minimum values of $\alpha_{VIS2.5}$ were 1.09 and 0.031 km^{-1}, respectively, and were higher than those of $\alpha_{IMAGE2.5}$.

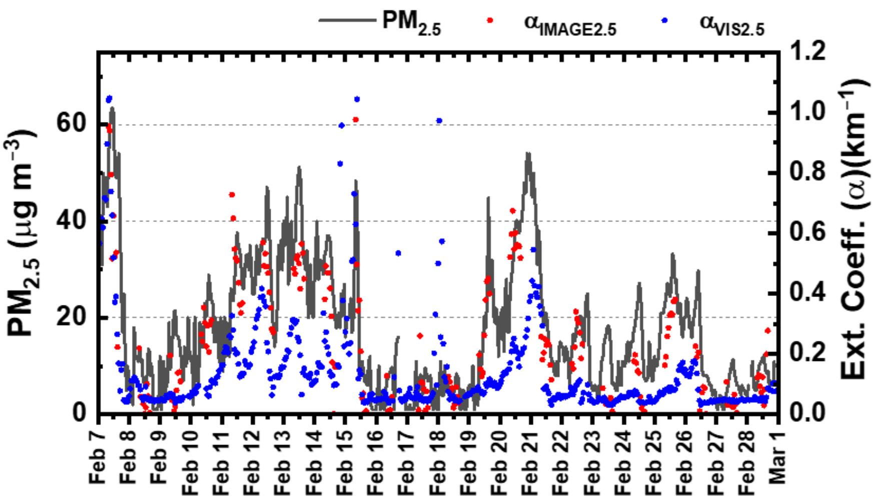

Figure 3. Mass concentrations of $PM_{2.5}$ (μg m^{-3}) and the extinction coefficients calculated from image pixels and visibility data during the measurement period.

The $PM_{2.5}$ mass concentrations were 6.0–21.5 μg m^{-3} in the maximum visibility range of 60 km for this measurement. The calculated $\alpha_{VIS2.5}$ on the maximum visibility varied from 0.031 to 0.041 km^{-1} depending on the atmospheric pressure and NO_2 concentration. Moreover, the range of $\alpha_{IMAGE2.5}$ was 0.004–0.15 km^{-1}. The minimum values of $\alpha_{IMAGE2.5}$ were considerably lower than those of $\alpha_{VIS2.5}$. Visibility can reach up to 300 km, when affected only by Rayleigh scattering and the gas absorption of air molecules [38], but the maximum visibility in this study was limited to 60 km. Therefore, we expected the $\alpha_{VIS2.5}$ to be overestimated on clear days.

Figure 4 shows the correlation between the mass concentration of $PM_{2.5}$, $\alpha_{IMAGE2.5}$, and $\alpha_{VIS2.5}$. The mass concentration of $PM_{2.5}$ has a high correlation with $\alpha_{IMAGE2.5}$ (R^2 = 0.70) (Figure 4a), which is larger than its correlation with $\alpha_{VIS2.5}$ (R^2 = 0.54 and 0.64 for linear and polynomial regression, respectively). In previous studies, the R^2 values between the extinction coefficients from lidar, satellite-based lidar, or visibility data and the mass concentration of $PM_{2.5,}$ measured by the in situ instrument, ranged from 0.50 to 0.96 [39–41]. The extinction coefficient calculated from mobile lidar on the vehicle was highly related to $PM_{2.5}$, with a relative humidity of 90% or lower (R^2 = 0.8) [39]. The mass concentration of $PM_{2.5}$ measured by the in situ instrument also has a significant relationship with the calculated value, and is classified into seven types (i.e., clean marine, dust, polluted, continental/smoke, clean continental, polluted dust, elevated smoke, and dusty marine) derived from the data of Cloud-Aerosol Lidar and Infrared Pathfinder Satellite Observation (CALIPSO), which is a satellite-based lidar [40]. Compared with previous studies, the correlation coefficient of 0.7 is low, which may be due to the short measurement period and relative humidity. This study had a limited measurement period of 22 days; therefore, the mass concentration range was narrow, ranging from 4.5 to 63.5 μg m^{-3}. The other studies, as mentioned above, measured the mass concentration of $PM_{2.5}$ for extended periods [40] or identified a varied mass concentration range of 200 μg m^{-3} [39]. In addition, we concluded that correction by relative humidity should be considered for a good correlation, as obtained in other studies.

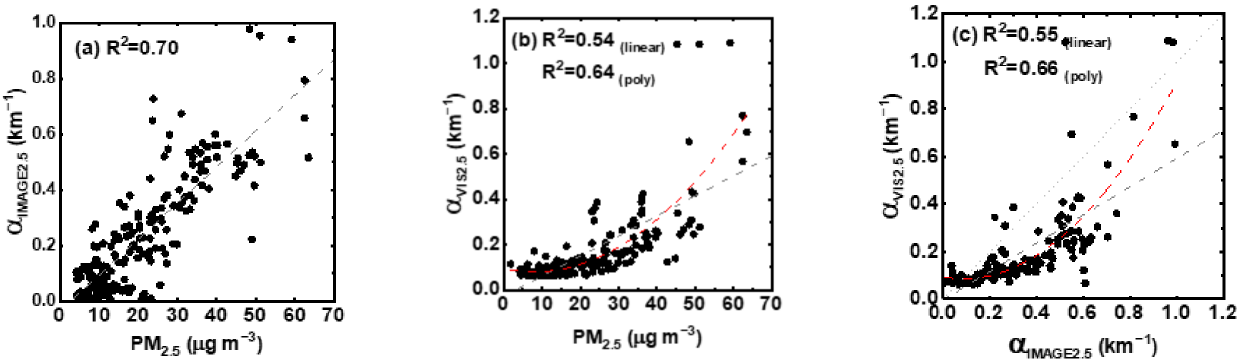

(**a**) (**b**) (**c**)

Figure 4. Correlation of the mass concentrations of $PM_{2.5}$ (μg m^{-3}) with the extinction coefficient obtained from (**a**) camera images ($\alpha_{IMAGE2.5}$) and (**b**) visibility data ($\alpha_{VIS2.5}$), and (**c**) of $\alpha_{IMAGE2.5}$ with $\alpha_{VIS2.5}$. The black dotted lines are from the linear regression method, and the red dotted lines are obtained from polynomial regression.

The correlation coefficient between the mass concentration of $PM_{2.5}$ and $\alpha_{VIS2.5}$ was low (0.54) compared with the correlation coefficient between the mass concentration of $PM_{2.5}$ and $\alpha_{IMAGE2.5}$ (0.70) using linear regression (Figure 4b). The correlation of $\alpha_{VIS2.5}$ and $\alpha_{IMAGE2.5}$ was also low (0.55); therefore, we could estimate light extinction by $PM_{2.5}$ with a higher accuracy using camera images than visibility data.

The differences between $\alpha_{VIS2.5}$ and $\alpha_{IMAGE2.5}$ might be due to several reasons. First, the error due to the large proportion of low $PM_{2.5}$ cases (52 cases among 193 cases) and the limitation of visual range at 60 km might cause these differences. Therefore, we believe that the visibility deduced from the extinction coefficient, that was calculated from the camera images, is more effective than that deduced using the visual method in person. Second, we did not consider the effects of relative humidity. Many studies confirmed that relative humidity has a high impact on visibility [30,35,36,42–46]. The correlation coefficient of the mass concentration of $PM_{2.5}$ and visibility data increased from 0.81 to 0.89 when correcting for the relative humidity [47]. Finally, deviations may occur due to the distance between the measurement site and the visibility observatory.

3.2. Mass Extinction Efficiency

The mass extinction efficiency (MEE) of $PM_{2.5}$ ($\alpha_{eff2.5}$) is a key parameter for confirming the extinction intensity per unit mass concentration. The light extinction by particulate matter is mainly related to hygroscopic deliquescence [48,49] while MEE is proportional to the relative humidity due to the increase in the water absorption capacity of aerosols [50,51].

In terms of the time-dependent changes in $\alpha_{eff2.5}$ and relative humidity (Figure 5), the calculated average values of $\alpha_{eff2.5}$ were (10.8 ± 6.9) $m^2\ g^{-1}$. The correlation between $\alpha_{eff2.5}$ and relative humidity was as low as 0.27 but it increased with the relative humidity (Figure 6). The $\alpha_{eff2.5}$ decreased on the dates of 10–11, 17–19, and 24–25 February, when the $PM_{2.5}$ concentrations were high. The $\alpha_{eff2.5}$ is an important factor that changes with various factors such as chemical composition, particle-size distribution, and refractive index. We found the particle-size distribution changed through $PM_{2.5}/PM_{10}$ ratio variations. The average $\alpha_{eff2.5}$ was higher than the measured values in previous other studies (Table 1) primarily conducted in China. One study measured the $\alpha_{eff2.5}$ in Busan, Korea, as 4.1–12.1 $m^2\ g^{-1}$ [46]. We attributed these differences to the influence of relative humidity. Water-soluble aerosol particles exist in solid form until the ambient relative humidity reaches the deliquescence relative humidity (DRH) threshold. The solid particles spontaneously absorb atmospheric moisture and their particle size rapidly increases on reaching the DRH, gradually converting them to a saturated aqueous solution. The DRH values vary with the ambient temperature and chemical species of aerosols [52,53]. A typical DRH value is 40% relative humidity [54]. In this study, the $\alpha_{eff2.5}$ decreased to (6.9 ± 5.0) $m^2\ g^{-1}$ for a DRH of 40%; however, it was higher than the values obtained in previous studies. Overall, the MEE of China and Korea is significantly different, which reflects that MEE is also an important parameter to determine the characteristics of aerosols.

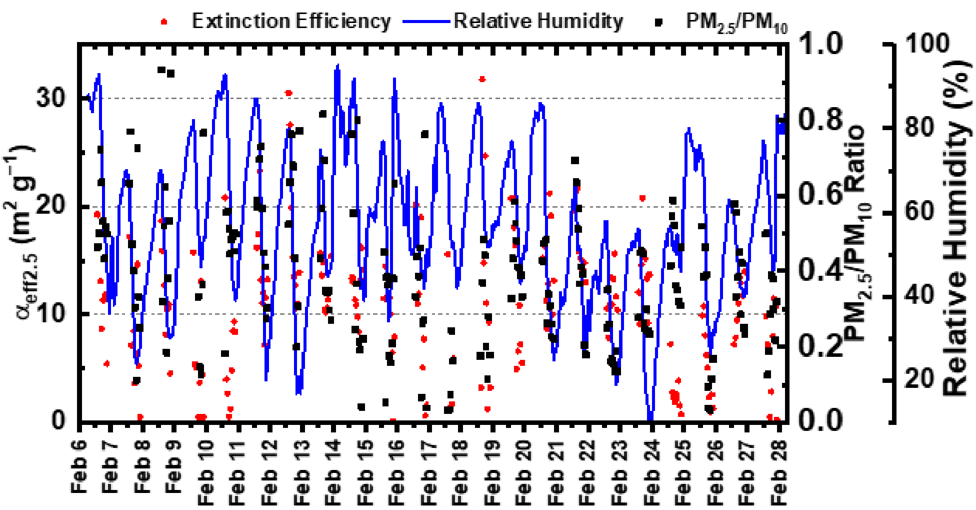

Figure 5. Mass extinction efficiency of $PM_{2.5}$ ($m^2\ g^{-1}$), relative humidity (%), and $PM_{2.5}/PM_{10}$ ratio during the measurement period.

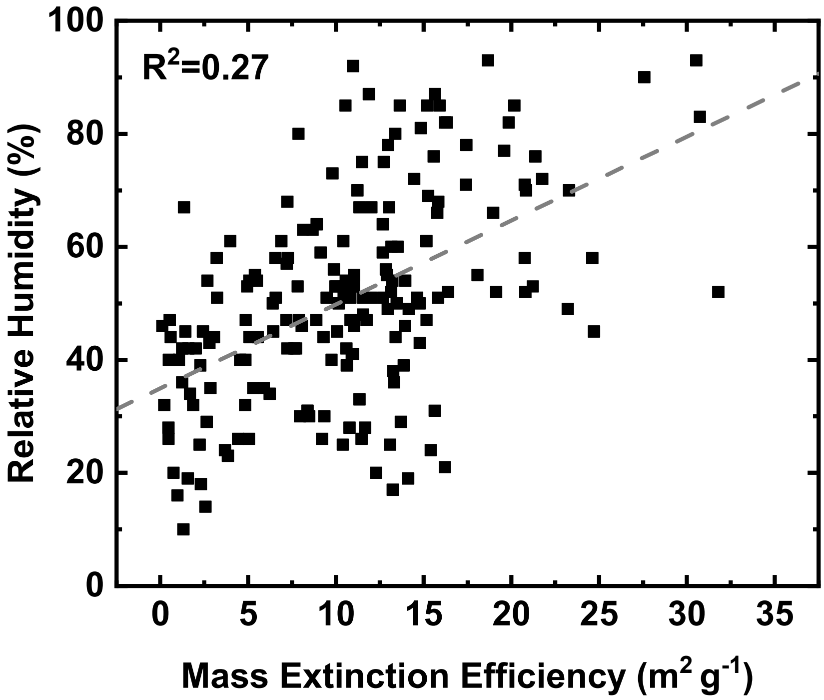

Figure 6. Relationship between mass extinction efficiency (m^2 g^{-1}) and relative humidity (%).

Table 1. Mass extinction efficiency (MEE) of $PM_{2.5}$.

Location	Year	MEE (m^2 g^{-1})	Reference
24 cities of China	2013–2014	4.4 ± 0.84	Cheng et al. (2017) [30]
YRD	2011–2012	4.1	Cheng et al. (2013) [35]
Eastern China	2014	5	He et al. (2016) [36]
Beijing	2006	4.3	Jung et al. (2009) [43]
Lin'an	1999	5	Xu et al. (2002) [42]
Beijing	2003–2008	4.7	Zhang et al. (2010) [34]
Nanjing	2013	7.1	Liu et al. (2020) [45]
	2018	9.3	
Busan, Korea	2015–2019	12.1 ± 8.3	Joo et al. (2021) [46]
Daejeon, Korea	2021	10.8 ± 6.9 (6.9 ± 5.0) [1]	This research

[1] denotes the limited cases in which the deliquescence relative humidity (DRH) is lower than 40%.

We inferred that the high values of $\alpha_{eff2.5}$ were caused by the changes in the size and composition of aerosols. Liu et al. [45] confirmed that the MEE in Nanjing, China, increased from 7.1 m^2 g^{-1} in 2013 to 9.3 m^2 g^{-1} in 2018. Joo et al. [46] also stated that the MEE of $PM_{2.5}$ increased by 0.72 m^2 g^{-1} annually during 2015–2019.

3.3. Diurnal Variation Patterns

The relative humidity exhibited regular variation patterns with maximum values from 5:00 to 8:00 h at approximately sunrise, then gradually decreased until approximately 15:00 h, and then increased again (Figure 5). The hourly change in the average mass concentration and the extinction coefficient of $PM_{2.5}$ depended on diurnal patterns (Figure 7). The mass concentration of $PM_{2.5}$, which had low values at 8:00 h, increased steadily, peaked at noon, and then decreased, indicating a minimum value at 16:00 h. In contrast, the extinction coefficient showed a maximum value at 08:00 h, then decreased until 16:00 h.

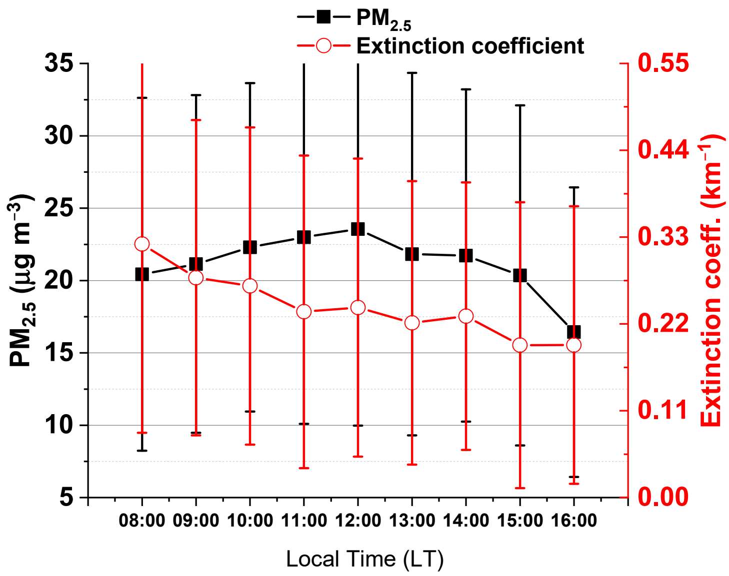

Figure 7. Diurnal patterns of $PM_{2.5}$ mass concentration (µg m^{-3}) and the extinction coefficient.

The daily change in the average values of $\alpha_{eff2.5}$, and the relative humidity for each time, are shown in Figure 8. The $\alpha_{eff2.5}$ exhibited a maximum value of (15.8 ± 5.9) m^2 g^{-1} at 8:00 h, decreased sharply to (11.3 ± 6.9) m^2 g^{-1} at 9:00 h, and then decreased slowly until 16:00 h. The relative humidity also had the highest value at 8:00 h, gradually decreased until 15:00 h, and increased from 16:00 h. From Figures 7 and 8, we confirmed that relative humidity had a significant effect on $\alpha_{eff2.5}$.

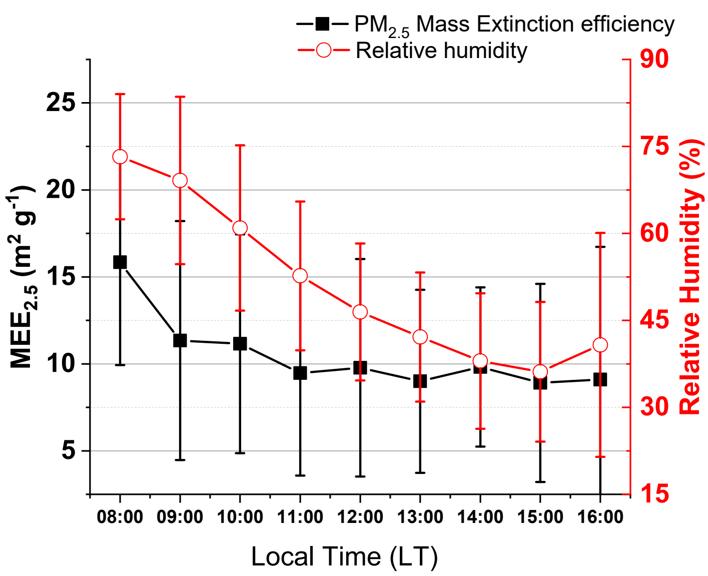

Figure 8. Diurnal patterns of the mass extinction efficiency of $PM_{2.5}$ ($MEE_{2.5}$) (m^2 g^{-1}) and relative humidity (%).

To verify the mass concentration of $PM_{2.5}$ calculated using $\alpha_{IMAGE2.5}$ and $\alpha_{eff2.5}$ applied from the camera images, we compared it with the in-situ measurement of $PM_{2.5}$. The $\alpha_{eff2.5}$ was applied as the overall average value of 10.8 m^2 g^{-1} in Figure 5 and the time average values in Figure 8. The correlation coefficient slightly increased from 0.71 to 0.73 when using the hourly data, but statistically significant results could not be evaluated (Figure 9). This might be because of the limited number of measurements; therefore, long-term observations and studies of seasonal characteristics must be conducted to obtain effective results in the future.

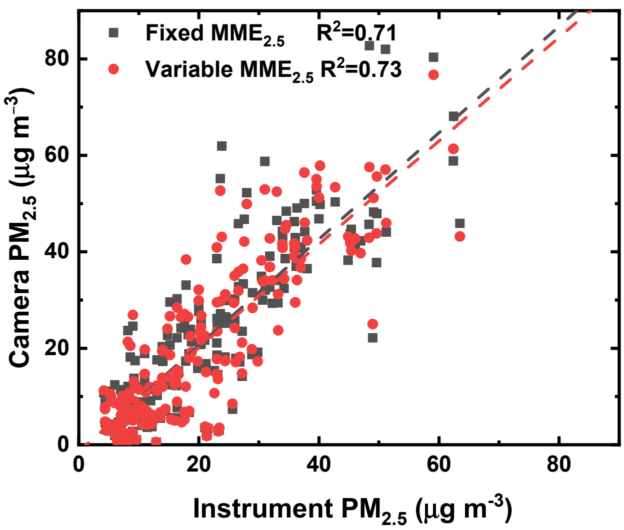

Figure 9. Correlation of the mass concentration of $PM_{2.5}$ ($\mu g\ m^{-3}$) measured by instrument and calculated from the camera images at fixed and variable mass extinction efficiency ($MEE_{2.5}$) values.

4. Conclusions

In this study, we calculated the extinction coefficient of $PM_{2.5}$ using the images captured by a commercial camera for the first time and confirmed its validity by comparing it with the extinction coefficient obtained from visibility data and the in-situ mass concentration of $PM_{2.5}$ measured instrumentally. The $\alpha_{IMAGE2.5}$ varied from 0.002 to 0.95 km^{-1} for $PM_{2.5}$ mass concentrations of 4.2–63.5 $\mu g\ m^{-3}$. The minimum and maximum values of $\alpha_{VIS2.5}$ were 1.09 km^{-1} and 0.031 km^{-1}, which were higher than those of $\alpha_{IMAGE2.5}$. The mass concentration of $PM_{2.5}$ was more correlated with $\alpha_{IMAGE2.5}$ (R^2 = 0.7) than with $\alpha_{VIS2.5}$ (R^2 = 0.54). We confirmed that the $\alpha_{eff2.5}$ was (10.8 $\pm$ 6.9) $m^2\ g^{-1}$, derived from the $\alpha_{IMAGE2.5,}$ and the $PM_{2.5}$ mass concentration was higher than the values from previous studies from Northeast Asia. Additionally, dry $\alpha_{eff2.5}$ (40 % DRH) was reduced to (6.9 $\pm$ 5.0) $m^2\ g^{-1}$.

We proved that the calculation of the $PM_{2.5}$ extinction coefficient using the images captured by a commercial camera had a high accuracy and could be used for research on changes in the atmosphere and the characteristics of aerosols. This implies that researchers can use camera images to identify atmospheric changes and particle characteristics caused by $PM_{2.5}$, not limited to visibility studies, by replacing the existing expensive optical measuring instruments. Moreover, the extinction coefficient and visibility can be calculated more effectively from the camera images than by using conventional methods. However, we only analyzed limited data for one month. Therefore, long-term and continuous observations must be conducted to verify the accuracy of the proposed method and to identify the independent properties of MEE.

Author Contributions: Conceptualization, Y.N.; methodology and software, Y.N. and D.K.; formal analysis and investigation, J.S.; writing—original draft preparation, J.S.; writing—review and editing, D.K.; supervision and project administration, Y.N.; funding acquisition, Y.N. All authors have read and agreed to the published version of the manuscript.

Funding: This work was supported by the "Graduate School of Particulate Matter Specialization" of Korea Environmental Industry & Technology Institute grant funded by the Ministry of Environment, Republic of Korea, and by the National Research Foundation of Korea (NRF) grant funded by the Korean government (MSIT, MOE) and (Grant No. 2019M3E7A1113103).

Institutional Review Board Statement: Not applicable.

Informed Consent Statement: Not applicable.

Data Availability Statement: The data presented in this study are available upon request from the corresponding author.

Acknowledgments: The authors would like to thank all members of the Atmospheric Environmental Remote Sensing Laboratory at Pukyong National University for their useful comments on this paper.

Conflicts of Interest: The authors declare no conflict of interest.

References

1. Brook, R.D.; Rajagopalan, S.; Pope, C.A., 3rd; Brook, J.R.; Bhatnagar, A.; Diez-Roux, A.V.; Holguin, F.; Hong, Y.; Luepker, R.V.; Mittleman, M.A.; et al. Particulate matter air pollution and cardiovascular disease: An update to the scientific statement from the American Heart Association. *Circulation* **2010**, *121*, 2331–2378. [CrossRef] [PubMed]
2. Kim, K.-H.; Kabir, E.; Kabir, S. A review on the human health impact of airborne particulate matter. *Environ. Int.* **2015**, *74*, 136–143. [CrossRef] [PubMed]
3. WHO. *The World Health Report 2006: Working Together for Health*; World Health Organization: Geneva, Switzerland, 2006.
4. WHO. *WHO 2021 Air Quality Guidelines*; World Health Organization: Geneva, Switzerland, 2021.
5. Amarillo, A.; Carreras, H.; Krisna, T.; Mignola, M.; Tavera Busso, I.; Wendisch, M. Exploratory analysis of carbonaceous PM2.5 species in urban environments: Relationship with meteorological variables and satellite data. *Atmos. Environ.* **2021**, *245*, 117987. [CrossRef]
6. Ma, Y.; Zhu, Y.; Li, H.; Jin, S.; Zhang, Y.; Fan, R.; Liu, B.; Gong, W. Estimation of the vertical distribution of particle matter (PM2.5) concentration and its transport flux from lidar measurements based on machine learning algorithms. *Atmos. Chem. Phys. Discuss.* **2021**, *21*, 17003–17016. [CrossRef]
7. Meskhidze, N.; Sutherland, B.; Ling, X.; Dawson, K.; Johnson, M.S.; Henderson, B.; Hostetler, C.A.; Ferrare, R.A. Improving Estimates of PM2.5 Concentration and Chemical Composition by Application of High Spectral Resolution Lidar (HSRL) and Creating Aerosol Types from Chemistry (CATCH) Algorithm. *Atmos. Environ.* **2021**, *250*, 118250. [CrossRef]
8. Stebel, K.; Stachlewska, I.S.; Nemuc, A.; Horálek, J.; Schneider, P.; Ajtai, N.; Diamandi, A.; Benešová, N.; Boldeanu, M.; Botezan, C.; et al. SAMIRA-SAtellite Based Monitoring Initiative for Regional Air Quality. *Remote Sens.* **2021**, *13*, 2219. [CrossRef]
9. Hollingsworth, A.; Engelen, R.; Textor, C.; Benedetti, A.; Boucher, O.; Chevallier, F.; Dethof, A.; Elbern, H.; Eskes, H.; Flemming, J. Toward a monitoring and forecasting system for atmospheric composition: The GEMS project. *Bull. Am. Meteorol. Soc.* **2008**, *89*, 1147–1164. [CrossRef]
10. Kim, J.; Kim, M.; Choi, M. Monitoring aerosol properties in east asia from geostationary orbit: GOCI, MI and GEMS. In *Air Pollution in Eastern Asia: An Integrated Perspective*; Springer: Berlin/Heidelberg, Germany, 2017; pp. 323–333.
11. Kim, M.; Kim, J.; Torres, O.; Ahn, C.; Kim, W.; Jeong, U.; Go, S.; Liu, X.; Moon, K.J.; Kim, D.-R. Optimal estimation-based algorithm to retrieve aerosol optical properties for GEMS measurements over Asia. *Remote Sens.* **2018**, *10*, 162. [CrossRef]
12. Kim, J.; Jeong, U.; Ahn, M.-H.; Kim, J.H.; Park, R.J.; Lee, H.; Song, C.H.; Choi, Y.-S.; Lee, K.-H.; Yoo, J.-M. New era of air quality monitoring from space: Geostationary Environment Monitoring Spectrometer (GEMS). *Bull. Am. Meteorol. Soc.* **2020**, *101*, E1–E22. [CrossRef]
13. Gultepe, I.; Müller, M.D.; Boybeyi, Z. A new visibility parameterization for warm-fog applications in numerical weather prediction models. *J. Appl. Meteorol. Climatol.* **2006**, *45*, 1469–1480. [CrossRef]
14. Muhammad, S.S.; Flecker, B.; Leitgeb, E.; Gebhart, M. Characterization of fog attenuation in terrestrial free space optical links. *Opt. Eng.* **2007**, *46*, 066001. [CrossRef]
15. Che, H.; Shi, G.; Uchiyama, A.; Yamazaki, A.; Chen, H.; Goloub, P.; Zhang, X. Intercomparison between aerosol optical properties by a PREDE skyradiometer and CIMEL sunphotometer over Beijing, China. *Atmos. Chem. Phys.* **2008**, *8*, 3199–3214. [CrossRef]
16. Olmo, F.J.; Cazorla, A.; Alados-Arboledas, L.; López-Álvarez, M.A.; Hernández-Andrés, J.; Romero, J. Retrieval of the optical depth using an all-sky CCD camera. *Appl. Opt.* **2008**, *47*, H182–H189. [CrossRef] [PubMed]
17. Huo, J.; Lü, D. Preliminary retrieval of aerosol optical depth from all-sky images. *Adv. Atmos. Sci.* **2010**, *27*, 421–426. [CrossRef]
18. Xu, X.; Shafin, S.H.; Li, Y.; Hao, H. A prototype system for atmospheric visibility estimation based on image analysis and learning. *J. Inf. Comput. Sci.* **2014**, *11*, 4577–4585. [CrossRef]
19. Song, H.; Chen, Y.; Gao, Y. Real-time visibility distance evaluation based on monocular and dark channel prior. *Int. J. Comput. Sci. Eng.* **2015**, *10*, 375–386. [CrossRef]
20. Guo, F.; Peng, H.; Tang, J.; Zou, B.; Tang, C. Visibility detection approach to road scene foggy images. *KSII Trans. Internet Inf. Syst.* **2016**, *10*, 4419–4441.
21. Saito, M.; Iwabuchi, H.; Murata, I. Estimation of spectral distribution of sky radiance using a commercial digital camera. *Appl. Opt.* **2016**, *55*, 415–424. [CrossRef]
22. Yu, Z.; Wang, J.; Liu, X.; He, L.; Cai, X.; Ruan, S. A new video-camera-based visiometer system. *Atmos. Sci. Lett.* **2019**, *20*, e925. [CrossRef]
23. Lee, K.H.; Kim, Y.J. Satellite remote sensing of Asian aerosols: A case study of clean, polluted, and Asian dust storm days. *Atmos. Meas. Tech.* **2010**, *3*, 1771–1784. [CrossRef]
24. Kim, D.; Noh, Y. An Aerosol Extinction Coefficient Retrieval Method and Characteristics Analysis of Landscape Images. *Sensors* **2021**, *21*, 7282. [CrossRef] [PubMed]

25. Narasimhan, S.G.; Nayar, S.K. Vision and the atmosphere. *Int. J. Comput. Vis.* **2002**, *48*, 233–254. [CrossRef]
26. Graves, N.; Newsam, S. Using visibility cameras to estimate atmospheric light extinction. In Proceedings of the 2011 IEEE Workshop on Applications of Computer Vision (WACV), Washington, DC, USA, 5–7 January 2011; pp. 577–584.
27. Park, S.; Kim, D. Aerosol-extinction Retrieval Method at Three Effective RGB Wavelengths Using a Commercial Digital Camera. *Korean J. Opt. Photonics* **2020**, *31*, 71–80. [CrossRef]
28. Bohren, C.F.; Huffman, D.R. *Absorption and Scattering of Light by Small Particles*; John Wiley & Sons: Hoboken, NJ, USA, 2008.
29. Koschmieder, H. Theorie der horizontalen sichtweite, Beitrage zur Physik der Freien Atmosphare. *Meteorol. Z.* **1924**, *12*, 3353.
30. Cheng, Z.; Ma, X.; He, Y.; Jiang, J.; Wang, X.; Wang, Y.; Sheng, L.; Hu, J.; Yan, N. Mass extinction efficiency and extinction hygroscopicity of ambient PM2.5 in urban China. *Env. Res* **2017**, *156*, 239–246. [CrossRef] [PubMed]
31. Larson, S.M.; Cass, G.R. Characteristics of summer midday low-visibility events in the Los Angeles area. *Environ. Sci. Technol.* **1989**, *23*, 281–289. [CrossRef]
32. Bucholtz, A. Rayleigh-scattering calculations for the terrestrial atmosphere. *Appl. Opt.* **1995**, *34*, 2765–2773. [CrossRef]
33. Pitchford, M.; Malm, W.; Schichtel, B.; Kumar, N.; Lowenthal, D.; Hand, J. Revised algorithm for estimating light extinction from IMPROVE particle speciation data. *J. Air Waste Manag. Assoc.* **2007**, *57*, 1326–1336. [CrossRef]
34. Zhang, Q.H.; Zhang, J.P.; Xue, H.W. The challenge of improving visibility in Beijing. *Atmos. Chem. Phys.* **2010**, *10*, 7821–7827. [CrossRef]
35. Cheng, Z.; Wang, S.; Jiang, J.; Fu, Q.; Chen, C.; Xu, B.; Yu, J.; Fu, X.; Hao, J. Long-term trend of haze pollution and impact of particulate matter in the Yangtze River Delta, China. *Environ. Pollut.* **2013**, *182*, 101–110. [CrossRef]
36. He, Q.; Zhou, G.; Geng, F.; Gao, W.; Yu, W. Spatial distribution of aerosol hygroscopicity and its effect on PM2.5 retrieval in East China. *Atmos. Res.* **2016**, *170*, 161–167. [CrossRef]
37. Hand, J.; Malm, W. Review of aerosol mass scattering efficiencies from ground-based measurements since 1990. *J. Geophys. Res. Atmos.* **2007**, *112*, D16203. [CrossRef]
38. Watson, J.G. Visibility: Science and regulation. *J. Air Waste Manag. Assoc.* **2002**, *52*, 628–713. [CrossRef]
39. Lv, L.; Liu, W.; Zhang, T.; Chen, Z.; Dong, Y.; Fan, G.; Xiang, Y.; Yao, Y.; Yang, N.; Chu, B. Observations of particle extinction, PM2. 5 mass concentration profile and flux in north China based on mobile lidar technique. *Atmos. Environ.* **2017**, *164*, 360–369. [CrossRef]
40. Ma, X.; Huang, Z.; Qi, S.; Huang, J.; Zhang, S.; Dong, Q.; Wang, X. Ten-year global particulate mass concentration derived from space-borne CALIPSO lidar observations. *Sci. Total Environ.* **2020**, *721*, 137699. [CrossRef]
41. Wang, Z.; Liu, C.; Dong, Y.; Hu, Q.; Liu, T.; Zhu, Y.; Xing, C. Profiling of Dust and Urban Haze Mass Concentrations during the 2019 National Day Parade in Beijing by Polarization Raman Lidar. *Remote Sens.* **2021**, *13*, 3326. [CrossRef]
42. Xu, J.; Bergin, M.; Yu, X.; Liu, G.; Zhao, J.; Carrico, C.; Baumann, K. Measurement of aerosol chemical, physical and radiative properties in the Yangtze delta region of China. *Atmos. Environ.* **2002**, *36*, 161–173. [CrossRef]
43. Jung, J.; Lee, H.; Kim, Y.J.; Liu, X.; Zhang, Y.; Gu, J.; Fan, S. Aerosol chemistry and the effect of aerosol water content on visibility impairment and radiative forcing in Guangzhou during the 2006 Pearl River Delta campaign. *J. Environ. Manag.* **2009**, *90*, 3231–3244. [CrossRef]
44. Zhang, X.Y.; Wang, Y.Q.; Niu, T.; Zhang, X.C.; Gong, S.L.; Zhang, Y.M.; Sun, J.Y. Atmospheric aerosol compositions in China: Spatial/temporal variability, chemical signature, regional haze distribution and comparisons with global aerosols. *Atmos. Chem. Phys.* **2012**, *12*, 779–799. [CrossRef]
45. Liu, J.; Ren, C.; Huang, X.; Nie, W.; Wang, J.; Sun, P.; Chi, X.; Ding, A. Increased Aerosol Extinction Efficiency Hinders Visibility Improvement in Eastern China. *Geophys. Res. Lett.* **2020**, *47*, e2020GL090167. [CrossRef]
46. Joo, S.; Naghmeh, D.; Noh, Y. A Study on the Characteristic Variations of Fine Particle in Busan and Ulsan through Particle Extinction Efficiency Analysis. *J. Korean Soc. Atmos. Environ.* **2021**, *37*, 80–90. [CrossRef]
47. Ji, D.; Deng, Z.; Sun, X.; Ran, L.; Xia, X.; Fu, D.; Song, Z.; Wang, P.; Wu, Y.; Tian, P.; et al. Estimation of PM2.5 Mass Concentration from Visibility. *Adv. Atmos. Sci.* **2020**, *37*, 671–678. [CrossRef]
48. Ding, Y.; Liu, Y. Analysis of long-term variations of fog and haze in China in recent 50 years and their relations with atmospheric humidity. *Sci. China Earth Sci.* **2014**, *57*, 36–46. [CrossRef]
49. Zhao, C.; Yu, Y.; Kuang, Y.; Tao, J.; Zhao, G. Recent progress of aerosol light-scattering enhancement factor studies in China. *Adv. Atmos. Sci.* **2019**, *36*, 1015–1026. [CrossRef]
50. Hyslop, N.P. Impaired visibility: The air pollution people see. *Atmos. Environ.* **2009**, *43*, 182–195. [CrossRef]
51. Liu, P.; Zhao, C.; Göbel, T.; Hallbauer, E.; Nowak, A.; Ran, L.; Xu, W.; Deng, Z.; Ma, N.; Mildenberger, K. Hygroscopic properties of aerosol particles at high relative humidity and their diurnal variations in the North China Plain. *Atmos. Chem. Phys.* **2011**, *11*, 3479–3494. [CrossRef]
52. Tang, M.; Chan, C.K.; Li, Y.J.; Su, H.; Ma, Q.; Wu, Z.; Zhang, G.; Wang, Z.; Ge, M.; Hu, M.; et al. A review of experimental techniques for aerosol hygroscopicity studies. *Atmos. Chem. Phys.* **2019**, *19*, 12631–12686. [CrossRef]
53. Seinfeld, J.H.; Pandis, S.N. *Thermodynamics of Aerosols. Atmospheric Chemistry and Physics: From Air Pollution to Climate Change*; John Wiley: Hoboken, NJ, USA, 2016; pp. 412–414.
54. Martin, S.T. Phase transitions of aqueous atmospheric particles. *Chem. Rev.* **2000**, *100*, 3403–3454. [CrossRef]